



Synthesis and characterization of g-C₃N₄/Bi₂MoO₆ heterojunctions with enhanced visible light photocatalytic activity



Haiping Li^a, Jingyi Liu^b, Wanguo Hou^{c,*}, Na Du^c, Renjie Zhang^c, Xutang Tao^a

^a State Key Laboratory of Crystal Materials, Shandong University, Jinan 250100, PR China

^b Environment Research Institute, Shandong University, Jinan 250100, PR China

^c Key Laboratory of Colloid and Interface Chemistry (Ministry of Education), Shandong University, Jinan 250100, PR China

ARTICLE INFO

Article history:

Received 26 February 2014

Received in revised form 1 May 2014

Accepted 11 May 2014

Available online 16 May 2014

Keywords:

g-C₃N₄

Bi₂MoO₆

Heterojunction

Composite

Photocatalytic

ABSTRACT

Heterojunctions of graphitic carbon nitride (g-C₃N₄) and Bi₂MoO₆ were solvothermally synthesized and characterized by X-ray diffraction, Fourier transform-infrared spectroscopy, X-ray photoelectron spectroscopy, scanning electron microscopy, transmission electron microscopy (TEM) and high resolution TEM. The photocatalytic degradation activity of the g-C₃N₄/Bi₂MoO₆ composites for Rhodamine B was examined under visible light irradiation. The heterojunction composites exhibited higher photocatalytic activity than pure g-C₃N₄ or Bi₂MoO₆. The photocatalytic activity of the composites increased then decreased with increasing Bi₂MoO₆ content. The g-C₃N₄/Bi₂MoO₆ heterojunction with a Bi₂MoO₆ content of 16.1 wt.% exhibited the highest photocatalytic activity, and its photocatalytic efficiency was more than three times those of pure g-C₃N₄ or Bi₂MoO₆. The enhanced photocatalytic activity of the g-C₃N₄/Bi₂MoO₆ heterostructure photocatalyst was attributed predominantly to the efficient separation of photoinduced electrons and holes. The g-C₃N₄/Bi₂MoO₆ heterojunction photocatalyst exhibited excellent stability and reusability. A detailed mechanism for the enhanced photocatalytic activity is discussed. Superoxide radicals were the major active species. This study provides a visible light responsive photocatalyst with potential in environmental remediation applications.

© 2014 Elsevier B.V. All rights reserved.

1. Introduction

Semiconductor-based photocatalysis is a promising green chemical technique, using sunlight as an energy source for pollutant degradation and hydrogen production from water splitting [1,2]. TiO₂ is an attractive photocatalyst, because of its wide availability and non-toxicity [3]. TiO₂ can only absorb ultraviolet light because of its large band gap (3.2 eV), which accounts for only 4% of the solar spectrum. This results in low photocatalytic activity under sunlight conditions. Numerous visible light active photocatalysts have been developed, including Bi-based [4], Ag-based [5], In-based [6], Cu-containing [7] and Co-containing [8] photocatalysts.

Graphitic carbon nitride (g-C₃N₄) is a recently reported metal-free polymeric semiconductor [9–12]. Its narrow band gap of 2.7 eV permits it to absorb visible light directly without modification. g-C₃N₄ exhibits high thermal and chemical stability, owing to its tri-s-triazine ring structure and high degree of condensation [12,13]. g-C₃N₄ exhibits high photocatalytic activity for

organic pollutant degradation [14] and hydrogen generation from water splitting [15,16], under visible light irradiation. However, its photocatalytic performance remains limited by the high recombination rate of photoinduced electrons and holes [17]. Efforts to improve the photocatalytic activity of g-C₃N₄ include designing appropriate textural properties [10,16,18], loading cocatalysts on the g-C₃N₄ surface [19], doping [20,21] and preparing composites or heterojunctions with other semiconductors [11,22]. Preparing heterojunctions with energetically matching conduction bands (CB) and valence bands (VB) is the most frequently used method. This is because heterojunction photocatalysts can allow faster separation of photoinduced charge carriers, resulting in much higher photocatalytic activities [11,17,22,23]. Reported g-C₃N₄-based heterojunctions include g-C₃N₄/CdS [9], g-C₃N₄/Fe₂O₃ [23], g-C₃N₄/Ag₃PO₄ [17], g-C₃N₄/Co₃O₄ [24], g-C₃N₄/CuInS₂ [25], g-C₃N₄/Ag₃VO₄ [26], g-C₃N₄/BiOBr [27] and g-C₃N₄/Bi₂WO₆ [28].

Bi₂MoO₆ is a layered Aurivillius-related oxide, consisting of [Bi₂O₂]²⁺ layers sandwiched between MoO₄²⁻ slabs. It is a semiconductor with a small band gap (2.5–2.8 eV), so is capable of capturing visible light. Bi₂MoO₆ exhibits photocatalytic activity for water splitting and organic pollutant degradation [29,30]. The practical application of Bi₂MoO₆ is limited by its poor quantum yield,

* Corresponding author. Tel.: +86 531 88365460; fax: +86 531 88364750.
E-mail address: wghou@sdu.edu.cn (W. Hou).

which is caused by the rapid recombination of photoinduced charge carriers. Bi_2MoO_6 -based heterojunctions have been prepared in attempt to decrease the recombination of charge carriers, and include TiO_2 - $\text{Bi}_2\text{MoO}_6/\text{Bi}_{3.64}\text{Mo}_{0.36}\text{O}_{6.55}$ [31], $\text{Bi}_2\text{O}_2\text{CO}_3/\text{Bi}_2\text{MoO}_6$ [32] and Bi_2MoO_6 /carbon nanofibers [33].

In the current study, the visible light active catalysts $\text{g-C}_3\text{N}_4$ and Bi_2MoO_6 were used to solvothermally prepare $\text{g-C}_3\text{N}_4/\text{Bi}_2\text{MoO}_6$ organic–inorganic heterojunctions, and $\text{g-C}_3\text{N}_4/\text{Bi}_2\text{MoO}_6$ was designed expecting to simultaneously reduce the recombination of photoinduced electrons and holes in $\text{g-C}_3\text{N}_4$ and Bi_2MoO_6 , thus enhancing photocatalytic performance. Favorable photodegradation efficiency of the heterojunction for Rhodamine B (RhB) was observed under visible light. Details of the photocatalytic mechanism are explored in this study. To the best of our knowledge, this is the first report on $\text{g-C}_3\text{N}_4/\text{Bi}_2\text{MoO}_6$ heterojunction photocatalysts with potential in environmental applications.

2. Experimental

2.1. Materials

Melamine, ethylene glycol, urea, ethylenediamine, sodium molybdate ($\text{Na}_2\text{MoO}_4 \cdot 2\text{H}_2\text{O}$) and bismuth nitrate ($\text{Bi}(\text{NO}_3)_3 \cdot 5\text{H}_2\text{O}$) were purchased from Aladdin (P.R. China), and P25 TiO_2 was purchased from Degussa (Germany). All chemicals were used as received without further purification. Water was obtained from a Hitech-Kflow water purification system (Hitech, P.R. China).

2.2. Preparation of $\text{g-C}_3\text{N}_4/\text{Bi}_2\text{MoO}_6$ heterojunction

$\text{g-C}_3\text{N}_4$ was prepared by directly heating melamine in a semi-closed system [23]. In detail, a known amount of melamine in a covered crucible was heated to 520°C in a muffle furnace at a heating rate of $20^\circ\text{C min}^{-1}$ over 2 h, and then retained at 520°C for 2 h.

To prepare the $\text{g-C}_3\text{N}_4/\text{Bi}_2\text{MoO}_6$ heterojunction, 1.8298–2.4381 g of as-prepared $\text{g-C}_3\text{N}_4$ was added to 0.3234 g of $\text{Bi}(\text{NO}_3)_3 \cdot 5\text{H}_2\text{O}$ in 10 mL of ethylene glycol. After sonification for 30 min, 0.0806 g of $\text{Na}_2\text{MoO}_4 \cdot 2\text{H}_2\text{O}$ was added to the dispersion, which was stirred for 1 h. The dispersion pH was then adjusted to 7.0 using ethylenediamine. After stirring for another 30 min, the dispersion was transferred to a 40-mL polytetrafluoroethylene-lined stainless autoclave, which was heated at 160°C for 6 h and then allowed to cool to room temperature. The solid product was collected by filtration, washed thoroughly with water and ethanol, and dried at 80°C . The target product was obtained by calcination at 400°C for 1 h to eliminate remained organic species.

For comparison, pure Bi_2MoO_6 was prepared similarly but without the addition of $\text{g-C}_3\text{N}_4$. As-prepared composites with expected Bi_2MoO_6 contents of 0 (pure $\text{g-C}_3\text{N}_4$), 4, 6, 8, 10 and 100% (pure Bi_2MoO_6) are referred to as A0, A4, A6, A8, A10 and A100, respectively. N-doped TiO_2 (N- TiO_2) and a mechanically mixed $\text{g-C}_3\text{N}_4/\text{Bi}_2\text{MoO}_6$ composite with a Bi_2MoO_6 content of 16.1% were also prepared for photocatalytic activity comparison (see supplementary data).

2.3. Characterization

Powder X-ray diffraction (XRD) was carried out using a D8 Advance diffractometer (Bruker, Germany), with Cu K_α radiation ($\lambda = 1.54184 \text{ \AA}$). Fourier transform-infrared (FT-IR) spectra were recorded on a Bruker Tensor 27 spectrophotometer (Germany). UV–vis diffuse reflectance spectra were obtained on a Cary 100 spectrophotometer (Agilent, USA), with a BaSO_4 reference. Thermogravimetric (TG) and differential scanning calorimetric (DSC) analyses were carried out on a SDT Q600 thermal analyzer (TA

Instruments, USA), by heating from 25 to 900°C , at a rate of 10°C/min in air. Elemental analyses were performed on a Vario El Cube elemental analyzer (Elementar, Germany). X-ray photoelectron spectroscopy (XPS) was performed on a Thermo Scientific Escalab 250Xi spectrometer (UK), with Al K_α radiation. The C 1s peak at 284.6 eV was used to calibrate peak positions. The composite structure was probed with transmission electron microscopy (TEM) and high-resolution TEM (HRTEM), using a Jeol JEM-2100F microscope (Japan). Morphologies were examined with a Supra55 field emission-scanning electron microscope (SEM) (Zeiss, USA). The spatial elemental distributions of composites were investigated by energy-dispersive spectrometry (EDS)-elemental mapping analysis, using an energy-dispersive X-ray spectrometer attached to the FE-SEM instrument. Photoluminescence (PL) spectra were measured using a Perkin-Elmer LS-55 fluorescence spectrometer (USA) with an excitation wavelength of 405 nm. Time-resolved fluorescence was measured using an Edinburgh Analytical Instrument FLS920 time-resolved spectrofluorometer (UK), using the time-correlated single-photon counting method, with an excitation wavelength of 405 nm. Specific surface areas and pore structures were probed by measuring volumetric N_2 adsorption–desorption isotherms at liquid nitrogen temperature, using an ASAP 2020 HD88 instrument (Micromeritics, USA). Samples were degassed at 200°C for 8 h under vacuum before measurements.

2.4. Photocatalytic activity

The photocatalytic performance of the as-prepared catalysts under visible light irradiation was evaluated by the degradation of RhB and methylene blue (MB) at room temperature on a XPA-7 photocatalytic reaction apparatus (Xujiang Electromechanical Plant, P.R. China). A 400-W metal halide lamp was used as the light source, and was equipped with an ultraviolet cutoff filter ($\lambda \geq 420 \text{ nm}$) to provide visible light. The distance between the lamp and reaction tubes containing dye solutions was about 10 cm. A water filter around the lamp was used to absorb infrared wavelengths. The tubes around the lamp are all soaked in a constant temperature bath. For each run, 0.02 g of photocatalyst was added to 50 mL of RhB (10 mg/L) or MB (5 mg/L) solution. Prior to irradiation, the suspension was treated by ultrasonication for 5 min, and then stirred in the dark for 1 h, to ensure sorption equilibrium. After a given irradiation time, $\sim 4 \text{ mL}$ aliquots of dye solutions were collected. These were centrifuged ($7100 \times g$) for 10 min and analyzed by a Hewlett–Packard 8453 UV–vis spectrophotometer (USA) at 554 and 664 nm for RhB and MB, respectively. The ratio of remaining dye concentration to its initial concentration, C/C_0 , was obtained by calculating the ratio of the corresponding absorbance. To evaluate the stability of the $\text{g-C}_3\text{N}_4/\text{Bi}_2\text{MoO}_6$ composites, recycling reactions were carried out for the photodegradation of RhB over composite A8 under visible light irradiation. After reaction, the photocatalyst was collected by centrifugation, washed, dried, and then used for the next run.

3. Results and discussion

3.1. XRD and FT-IR analyses

XRD was used to identify the crystal structures of the as-prepared samples. As shown in Fig. 1, two distinct peaks at 13.0 and 27.6° for pure $\text{g-C}_3\text{N}_4$ (A0) can be indexed to the (100) and (002) diffraction planes of graphite-like carbon nitride [28], respectively. These correspond to the in-plane structural packing motif and interlayer stacking of aromatic segments [28,34]. In the XRD pattern of pure Bi_2MoO_6 (A100), diffraction peaks at 28.3 , 32.5 , 47.2 and 55.5° correspond to the (131), (002), (062)

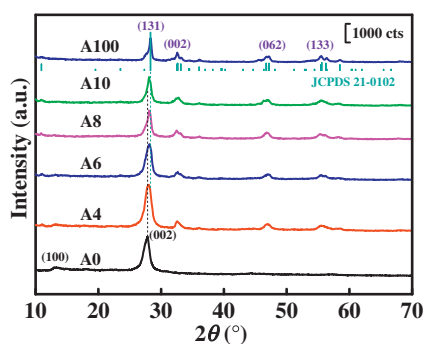


Fig. 1. XRD patterns of g-C₃N₄ (A0), Bi₂MoO₆ (A100) and g-C₃N₄/Bi₂MoO₆ composites (A4–A10).

and (133) planes, respectively. These can be indexed as pure orthorhombic Bi₂MoO₆ (JCPDS file 21-0102, $a = 5.506$, $b = 16.226$ and $c = 5.487$ Å). No peaks indicating impurities were observed. For the g-C₃N₄/Bi₂MoO₆ composites A4–A10, all diffraction peaks of Bi₂MoO₆ are clearly observed, indicating that the solvothermal process did not influence the crystal structure of Bi₂MoO₆. With increasing Bi₂MoO₆ content, the (100) peak of g-C₃N₄ gradually decreases in intensity, and the (002) peak overlaps with the (131) peak of Bi₂MoO₆.

The FT-IR spectra of g-C₃N₄, Bi₂MoO₆ and their composites are shown in Fig. 2. In the spectrum of g-C₃N₄, several absorption bands at 1800–890 cm^{−1} are attributed to either C=N or C–N stretching vibrations [26,35]. The broad adsorption band centered at 3176 cm^{−1} is ascribed to the N–H stretching vibration [30]. The band at 808 cm^{−1} is associated with the characteristic breathing mode of s-triazine [26,30]. In the spectrum of Bi₂MoO₆, peaks at 3443 and 1636 cm^{−1} are attributed to O–H vibrations [36]. Absorption bands at 910–650 cm^{−1} and 630–430 cm^{−1} are attributed to Mo–O stretching vibrations and Bi–O stretching and deformation vibrations [37], respectively. Absorption bands of g-C₃N₄ are apparent in the spectra of g-C₃N₄/Bi₂MoO₆ composites, while those of Bi₂MoO₆ are not, because of the low content of Bi₂MoO₆.

3.2. XPS analysis

The surface chemical composition of g-C₃N₄, g-C₃N₄/Bi₂MoO₆ composite A8 and Bi₂MoO₆, and the interaction between g-C₃N₄ and Bi₂MoO₆ were analyzed by XPS. Fig. 3 shows XPS survey spectra and high-resolution XPS spectra of the C 1s, N 1s, Bi 4f, Mo 3d and O 1s regions for these three samples. The survey spectra of A0, A8 and A100 indicate that C, N and O exist on the surface of g-C₃N₄,

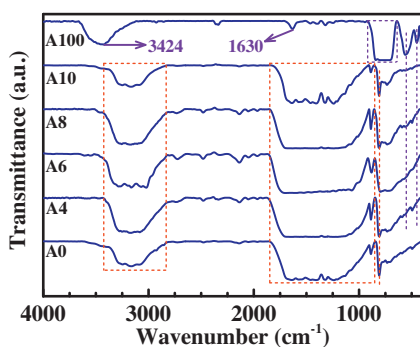


Fig. 2. FT-IR spectra of g-C₃N₄ (A0), Bi₂MoO₆ (A100) and g-C₃N₄/Bi₂MoO₆ composites (A4–A10).

Bi, Mo, O and C on the surface of Bi₂MoO₆, and C, N, Bi, Mo and O on the surface of A8. The C 1s peak in the survey spectrum of Bi₂MoO₆ results from adventitious carbon [33]. The O 1s peak in the survey spectrum of g-C₃N₄ is assigned to adsorb H₂O on the photocatalyst surface [35]. In the C 1s high-resolution XPS spectrum of g-C₃N₄, the peak at 284.6 eV arises from external carbon contamination [26]. The peak at 287.9 eV is related to coordination between carbon atoms and three nitrogen atoms in the g-C₃N₄ lattice [26,35]. The broad N 1s peak in the spectrum of g-C₃N₄ is deconvoluted into three component peaks. The first at 398.3 eV is due to the sp² N of triazine rings and the tertiary nitrogen N–(C)₃ [35]. The second at 399.9 eV is attributed to –NH₂ or =NH groups [35]. The third at 404.2 eV is due to charging effects or positive charge localization in heterocycles [38]. For A8, the peak positions of C 1s and N 1s are similar to those of pure g-C₃N₄, except for the occurrence of the Mo 3p_{3/2} peak in the N 1s spectrum. In the Bi 4f spectra, peaks at 158.9 and 164.2 eV for Bi₂MoO₆ are attributed to Bi 4f_{7/2} and Bi 4f_{5/2} of Bi³⁺, respectively [39]. Those peaks in the spectrum of A8 shift to 159.3 and 164.6 eV, respectively, being 0.4 eV higher than those of Bi₂MoO₆. In the Mo 3d spectrum of Bi₂MoO₆, peaks at 232.1 and 235.3 eV are ascribed to Mo 3d_{5/2} and Mo 3d_{3/2} of Mo⁶⁺, respectively, and are 0.3 eV lower than the corresponding two peaks in the Mo 3d spectrum of A8. In the O 1s spectra, wide asymmetric peaks of Bi₂MoO₆ and A8 can be deconvoluted into three component peaks. Those at 529.5, 530.2 and 531.5 eV for Bi₂MoO₆ are related to Bi–O, Mo–O and surface hydroxyl groups (O–H) [33,39], respectively. The Bi–O and M–O binding energies in A8 are 0.4 and 0.3 eV higher than those in Bi₂MoO₆, respectively. The binding energies of Bi 4f, Mo 3d and O 1s of A8 are all higher than those of Bi₂MoO₆. This could be attributed to the interaction between g-C₃N₄ and Bi₂MoO₆ [26], or the formation of g-C₃N₄/Bi₂MoO₆ heterojunctions.

3.3. TG and elemental analyses

Elemental analyses (EA) of composites A0–A10 are listed in Table 1. The N/C ratios of all composites are about 1.49, indicating that the elemental composition of g-C₃N₄ was constant during preparation. The detected minor hydrogen content (~1.8 wt.%) is due to the presence of uncondensed amino groups and surface-adsorbed water [35]. The Bi₂MoO₆ contents of the composites are significantly higher than the ideal contents calculated from raw material ratios. Similar results have been reported for g-C₃N₄/SmVO₄ [40]. This probably results from the partial decomposition of g-C₃N₄ during preparation.

Fig. 4 shows the TG-DSC results of g-C₃N₄ and g-C₃N₄/Bi₂MoO₆ composites. The TG curve of pure g-C₃N₄ exhibits a single sharp weight loss at 744 °C. The TG-DSC curves of g-C₃N₄/Bi₂MoO₆ composites differ from those of pure g-C₃N₄. Two exothermal peaks at approximately 514 ± 5 and 549 ± 8 °C appear in the DSC curves of A4–A10. This indicates that the thermal stability of the composites is lower than that of pure g-C₃N₄. The major exothermal peaks of the composites are much higher than that of pure g-C₃N₄, probably because of the weight loss of pure g-C₃N₄ partly arising from sublimation [40]. More g-C₃N₄ is oxidized in the presence of Bi₂MoO₆, because of Bi₂MoO₆ adsorbing and activating atmospheric oxygen, which results in the exothermal peak increase of the composites. Similar results have been reported for the g-C₃N₄/SmVO₄ composite [40]. The increasing degree of g-C₃N₄ oxidation in the composites leads to a decrease in their thermal stability. Pure g-C₃N₄ (A0) can be eliminated completely in the temperature range studied (Fig. 4). The total weight loss of A4–A10 is <100 wt.%, because Bi₂MoO₆ is not decomposed to any degree (Fig. S1). Therefore, the Bi₂MoO₆ contents of the composites can be calculated from the TG data, as shown in Table 1. The results are comparable with those from the EA data.

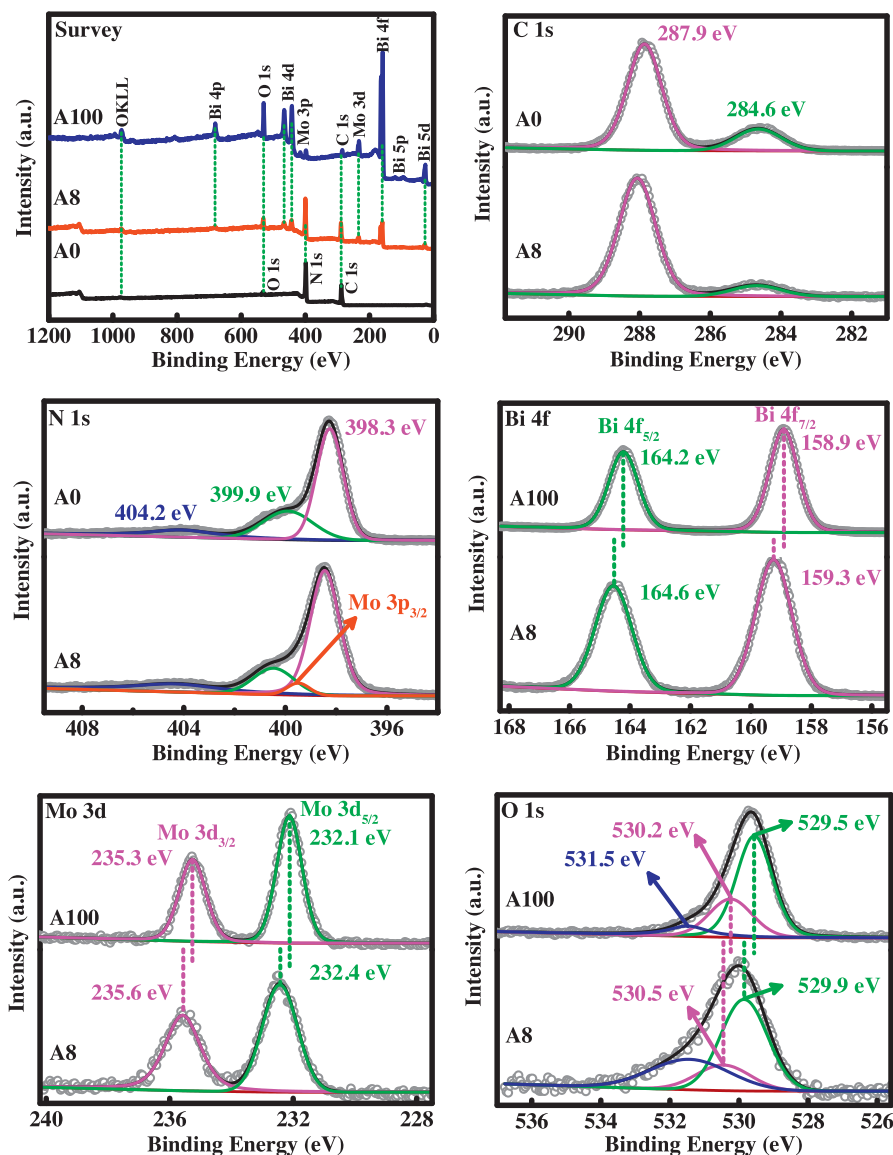


Fig. 3. XPS survey spectra and high-resolution XPS spectra of the C 1s, N 1s, Bi 4f, Mo 3d and O 1s regions for g-C₃N₄ (A0), Bi₂MoO₆ (A100) and the g-C₃N₄/Bi₂MoO₆ composite A8.

3.4. Morphology

Figs. 5 and 6 show SEM and TEM images, respectively, of g-C₃N₄, Bi₂MoO₆ and their composite A8. Large aggregates composed of lamellar structures are observed for g-C₃N₄ (Figs. 5a and 6a). Hierarchically hollow spheres are observed for pure Bi₂MoO₆ (Fig. 5b). The layered structure of g-C₃N₄ still exists in the composite (Figs. 5c, f and 6b, c), but the hierarchically hollow spheres of Bi₂MoO₆ are not readily observed (Fig. 5c and f). Many irregular particles or particle aggregates sized from several tens of nanometers to

micrometers are observed adhering to the surface of g-C₃N₄ (Figs. 5c, d, f and 6b and c). EDS indicates the existence of C, N, Bi, Mo and O in A8 (Fig. 5e), in accordance with the XPS result. The elemental mapping images show a relatively homogeneous distribution of Bi₂MoO₆ on the g-C₃N₄ surface (Fig. 5g). The large Bi₂MoO₆ particles in the enclosed area in Fig. 5f are clearly mirrored at the same positions in the Bi, Mo and O mapping images (Fig. 5g), as marked by the circles. HRTEM images in Fig. 6d and e show the anchoring of Bi₂MoO₆ nanoparticles on the g-C₃N₄ surface, and distinct lattice fringes are observed. Fringes spaced

Table 1
Elemental analyses of g-C₃N₄ and g-C₃N₄/Bi₂MoO₆ composites.

Sample	N/C molar ratio	H content (wt.%)	Bi ₂ MoO ₆ content (wt.%)		
			EA	TG	Ideal
A0	1.47	2.1	0	0	0
A4	1.49	2.0	4.9	5.6	4
A6	1.49	1.8	10.5	11.5	6
A8	1.49	1.8	16.1	16.6	8
A10	1.50	1.6	18.5	20.6	10

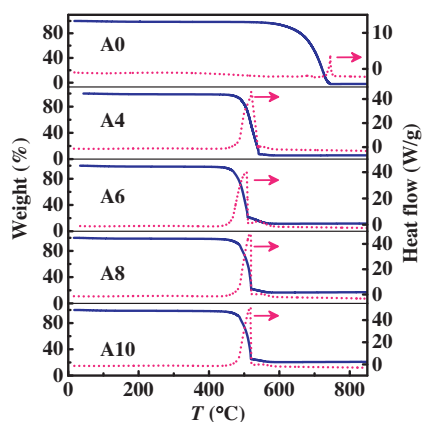


Fig. 4. TG-DSC analyses for g-C₃N₄ and g-C₃N₄/Bi₂MoO₆ composites.

by ~ 0.192 and ~ 0.275 nm in Fig. 6d, and by ~ 0.315 , ~ 0.157 and ~ 0.327 nm in Fig. 6e correspond to the (062), (200), (131), (262) and (140) planes of Bi₂MoO₆, respectively. The lattice fringes of g-C₃N₄ in the composite are difficult to observe because of the

very weak two-dimensional ordering of g-C₃N₄ [28], as indicated by its indistinct in-plane diffraction (100) (Fig. 1). The SAED image clearly shows the existence of several diffraction spots (Fig. 6f). Both the SAED and lattice fringe images (Fig. 6e and f) indicate that the observed Bi₂MoO₆ particles consist of several single crystals. The tight coupling between g-C₃N₄ and Bi₂MoO₆, as shown in Fig. 6d and e, demonstrates the formation of g-C₃N₄/Bi₂MoO₆ heterojunctions.

3.5. N₂ adsorption–desorption isotherms

Fig. 7a shows N₂ adsorption–desorption isotherms of g-C₃N₄, Bi₂MoO₆ and their composite A8. All isotherms are of type IV, which is usually associated with capillary condensation in mesopores [41]. The type H3 hysteresis loops at high P/P_0 reflect the formation of slit-shaped pores from aggregates of particles [42]. The Brunauer–Emmett–Teller (BET) specific surface area of A8 is 39.6 m²/g, which is higher than those of g-C₃N₄ and Bi₂MoO₆ at 17.4 and 12.1 m²/g, respectively. The pore-size distributions of the samples are estimated using the Barrett–Joyner–Halenda (BJH) method from the adsorption branches, as shown in Fig. 7b. Bimodal pore-size distributions are observed for all samples, and the two most

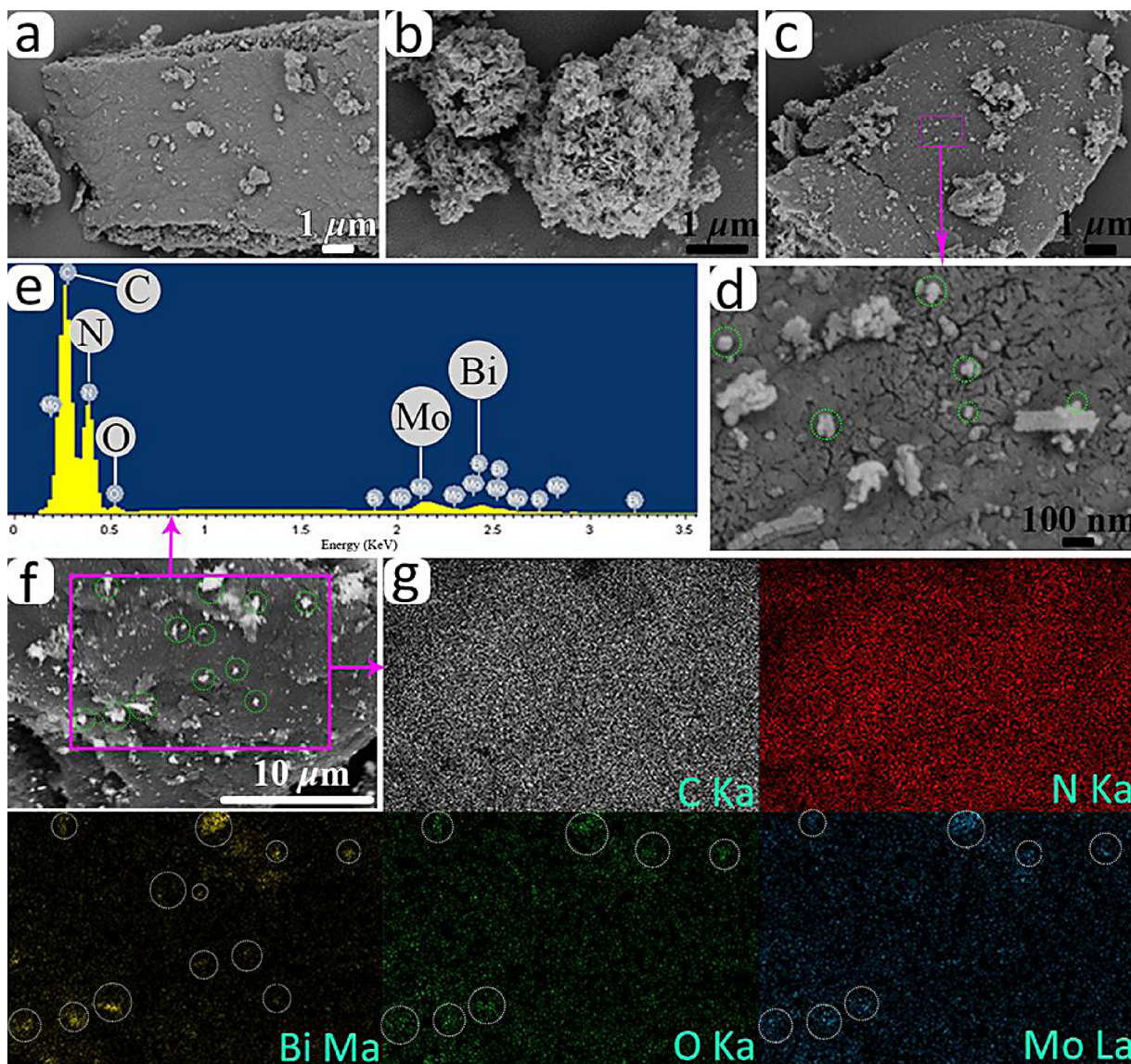


Fig. 5. SEM images of (a) g-C₃N₄, (b) Bi₂MoO₆ and (c, d and f) g-C₃N₄/Bi₂MoO₆ composite A8, and (e) EDS spectrum and (g) corresponding elemental mapping images of A8.

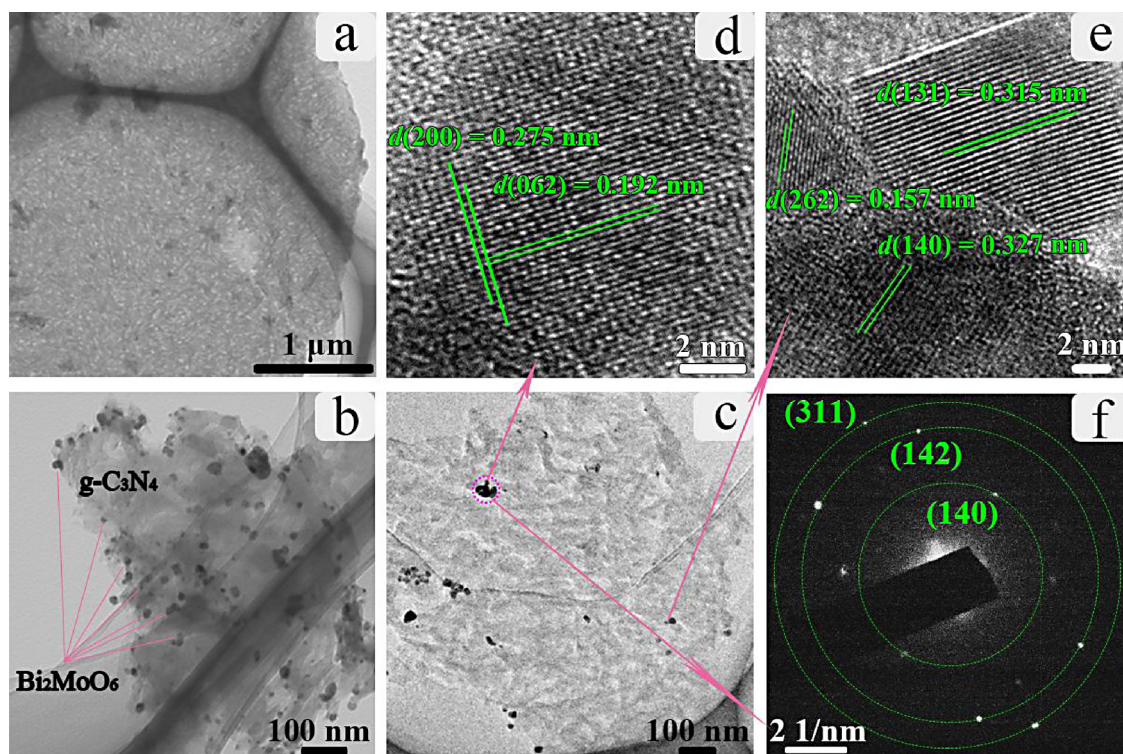


Fig. 6. TEM images of (a) g-C₃N₄ and (b, c) g-C₃N₄/Bi₂MoO₆ composite A8, and (d, e) HRTEM and (f) SAED images of A8.

probable pore diameters of g-C₃N₄, A8 and Bi₂MoO₆ are ~2.8 and ~30.6 nm, ~2.6 and ~30.4 nm, and ~2.3 and ~43.9 nm, respectively. All of these are characteristic of mesopores (2–50 nm). Compared with Bi₂MoO₆ and g-C₃N₄, the pore size and distribution of A8 exhibit no obvious changes, but the pore volume of A8 is 0.21 cm³/g, which is slightly larger than those of g-C₃N₄ and Bi₂MoO₆ at 0.15 and 0.09 cm³/g, respectively. The high specific surface area and pore volume are likely to contribute to an enhancement in photocatalytic activity.

3.6. Photocatalytic activity

The visible light photocatalytic activity of as-prepared g-C₃N₄, Bi₂MoO₆ and their composites was evaluated through the

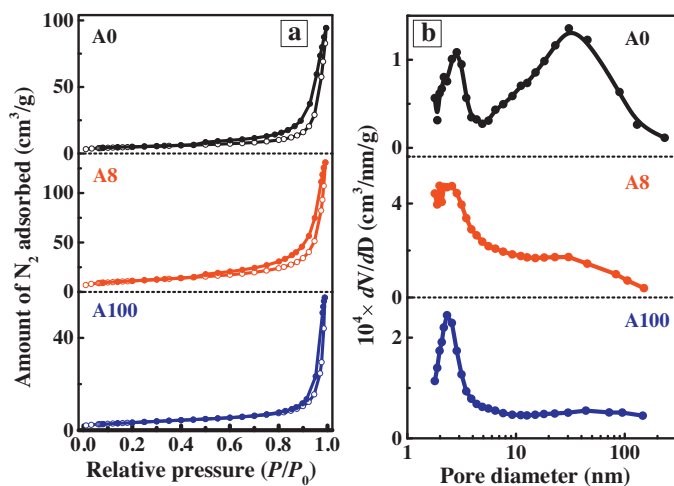


Fig. 7. (a) N₂ adsorption-desorption isotherms and (b) pore-size distribution curves for g-C₃N₄ (A0), Bi₂MoO₆ (A100) and g-C₃N₄/Bi₂MoO₆ composite A8.

degradation of RhB in aqueous solution. Adsorption equilibrium is reached for all photocatalysts tested, after stirring for 1 h in the dark (Figs. S2 and S3a). As shown in Fig. 8, the absorption of RhB in the visible light region significantly decreases with increasing irradiation time. No corresponding increase in absorption is observed in the ultraviolet region, which indicates the complete destruction of most aromatic structures. The maximum absorption wavelength exhibits a blue shift, as reported in the literature [43]. Fig. 9a shows that when the solution is irradiated with visible light for 70 min in the absence of any catalyst, little change in RhB concentration is observed. This indicates that the self-photodegradation of RhB is negligible [23]. As the Bi₂MoO₆ content in the composites increases from 0 to 18.5 wt.%, the photocatalytic activity of the g-C₃N₄/Bi₂MoO₆ composites gradually increases, and then decreases, with A8 exhibiting the highest activity (Fig. 9a). The photoactivity of A8 is higher than those of g-C₃N₄, Bi₂MoO₆, commercial P25 TiO₂, N-TiO₂ and the mechanically mixed g-C₃N₄/Bi₂MoO₆ composite (Fig. 9a and b). After 70 min, about 98% of RhB is removed by composite A8, while less than <60% is removed by pure g-C₃N₄ or Bi₂MoO₆.

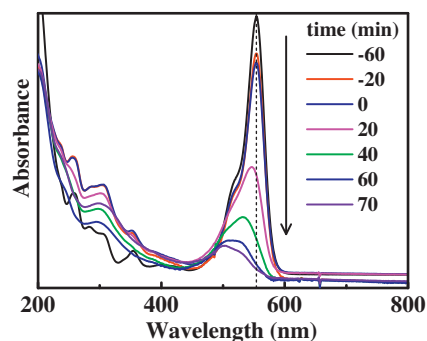


Fig. 8. Absorption spectra of RhB after different irradiation times in the presence of g-C₃N₄/Bi₂MoO₆ composite A8.

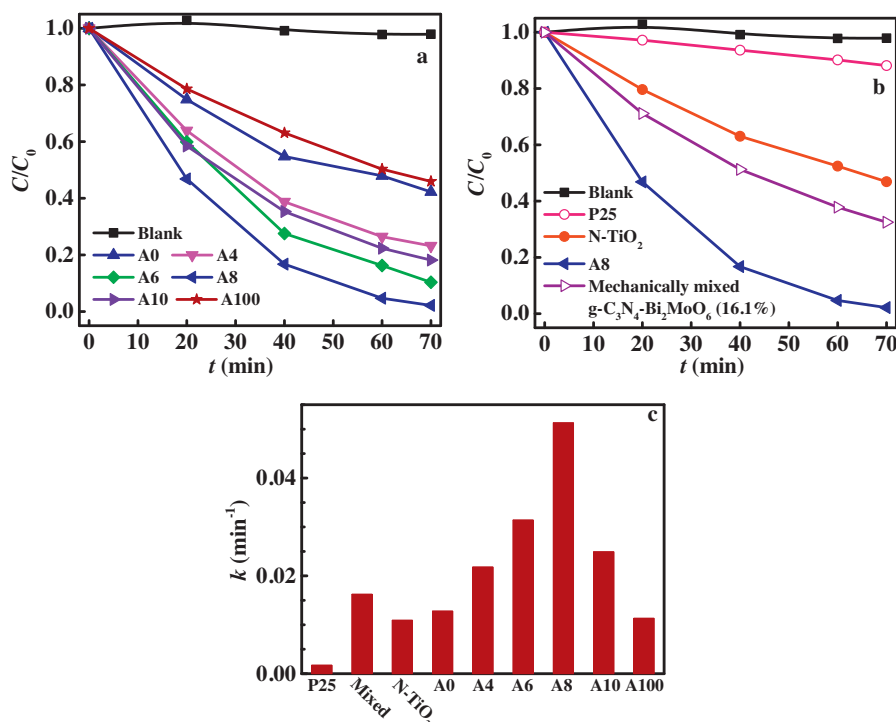


Fig. 9. (a, b) RhB degradation over various photocatalysts and (c) corresponding rate constants (k).

To quantitatively investigate the reaction kinetics of RhB photodegradation by the as-prepared samples, the experimental data were fitted to the pseudo-first-order model, $-\ln(C/C_0) = kt$, where k is the apparent first-order rate constant. All plots of $-\ln(C/C_0)$ against t exhibit linear trends (Fig. S4), indicating that the RhB photodegradation process is satisfactorily described by the pseudo-first-order model. The k values of samples A0–A100 are shown in Fig. 9c. The k values gradually increase, and then decrease, with increasing Bi₂MoO₆ content. A8 exhibits the maximum k , which is more than three times those of g-C₃N₄ or Bi₂MoO₆ (Fig. 9c).

The photodegradation of MB over the as-prepared photocatalysts was also investigated (Fig. S3). The photodegradation efficiency for MB exhibits similar trends with increasing composite Bi₂MoO₆ content to those for RhB. The photocatalytic activity of A8 is 0.5 times higher than that of g-C₃N₄, and twice that of Bi₂MoO₆. In addition, MB itself exhibits a relatively high photodegradation efficiency under visible light irradiation (Fig. S4).

The stability of photocatalysts is crucial for their practical application. Fig. 10 shows that after six consecutive runs, no apparent deactivation of the composite A8 is observed, and the RhB degradation efficiency declines by <1%. XRD patterns of A8 before and after

photocatalytic reaction indicate that its crystal structure remains constant throughout the reaction (Fig. S5). The as-synthesized g-C₃N₄/Bi₂MoO₆ heterojunction photocatalyst exhibits excellent stability in the visible light photochemical degradation reactions.

3.7. Photocatalytic mechanism

UV–vis diffusive reflectance spectra of g-C₃N₄, Bi₂MoO₆ and their composites indicate that all samples exhibit photoabsorption properties from the UV to visible regions (Fig. S6). The absorption edge of Bi₂MoO₆ is ~500 nm, and the corresponding band gap energy (E_g) is ~2.48 eV. The composites A4–A10 exhibit a similar absorption edge (~467 nm) to g-C₃N₄, and their corresponding E_g is ~2.66 eV. This is comparable to the ideal value (2.7 eV) of g-C₃N₄ [9,28]. The CB bottom and VB top potentials (E_{CB} and E_{VB} , respectively) of g-C₃N₄ are at −1.13 and +1.57 eV [22], respectively. Those of Bi₂MoO₆ are estimated to be at −0.19 and +2.29 eV, respectively, according to the empirical equation $E_{VB} = X - E^e + 0.5E_g$ [44], where X is the electronegativity of the semiconductor, which is the geometric mean of the electronegativity of the constituent atoms, and E^e is the energy of free electrons on the hydrogen scale (about 4.5 eV). The X value of Bi₂MoO₆ is 5.55 eV [45].

Both g-C₃N₄ and Bi₂MoO₆ are *n*-type semiconductors [31,46]. Before contact, the CB edge of Bi₂MoO₆ is lower than that of g-C₃N₄, and the Fermi level (E_F) of Bi₂MoO₆ is also lower than that of g-C₃N₄. After contact, the electrons diffuse from g-C₃N₄ to Bi₂MoO₆, and the E_F of Bi₂MoO₆ increases while the E_F of g-C₃N₄ decreases until an equilibrium state is formed [46]. Corresponding with the increasing and/or decreasing of the E_F , the whole energy bands of Bi₂MoO₆ are increased while those of g-C₃N₄ are decreased. The probable energy band structure of the equilibrium state g-C₃N₄/Bi₂MoO₆ heterojunction is shown in Scheme 1. At equilibrium, the inner electric field is formed. The g-C₃N₄ region has positive charges while Bi₂MoO₆ has negative charges. Under visible light irradiation, both g-C₃N₄ and Bi₂MoO₆ absorb photons with energy greater than their corresponding band gaps, which excites electrons to the CB and leaves holes in the VB. Although the transfer of electrons from the

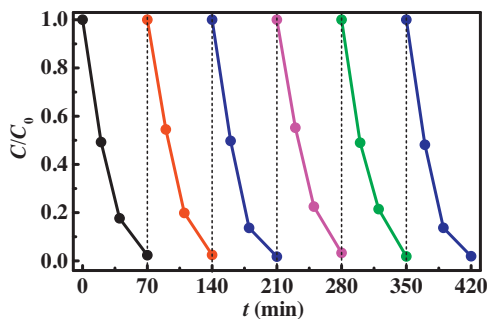
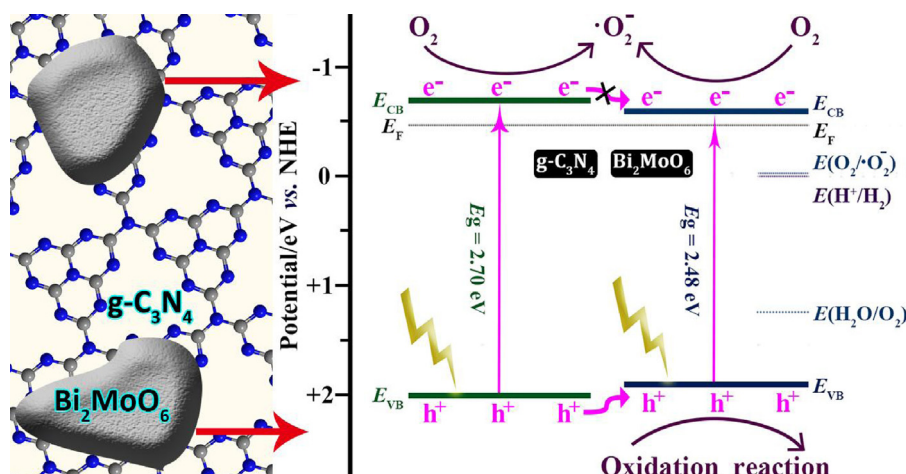


Fig. 10. Cycling runs for photocatalytic degradation of RhB over g-C₃N₄/Bi₂MoO₆ composite A8 under visible light irradiation.



Scheme 1. Schematic diagram of the separation and transfer of photogenerated charges in the g-C₃N₄/Bi₂MoO₆ heterojunction under visible light irradiation.

CB of g-C₃N₄ to the CB of Bi₂MoO₆ is prohibited because of the inner electric field, the transfer of holes from the VB of g-C₃N₄ to the VB of Bi₂MoO₆ is promoted (Scheme 1). This effectively reduces the recombination of photoinduced electrons and holes, resulting in enhanced photodegradation efficiency.

PL spectra are useful for revealing the transfer and separation efficiency of photogenerated charge carriers [35]. Higher PL intensity indicates a higher recombination of charge carriers [46]. PL spectra of g-C₃N₄, Bi₂MoO₆ and their composites A4–A10 are shown in Fig. 11. The main emission peak is centered at about 460 nm for pure g-C₃N₄, which is in agreement with reported results [24]. Compared with g-C₃N₄, the addition of Bi₂MoO₆ hardly changes the emission peak position, but rather reduces its relative intensity. This indicates that the formation of the g-C₃N₄/Bi₂MoO₆ heterojunction contributes to the separation of photoinduced charge carriers.

The recombination kinetics of photoinduced charge carriers in g-C₃N₄, Bi₂MoO₆, and A8 were investigated by time-resolved fluorescence spectroscopy. The fluorescence intensity at 460 nm was monitored upon excitation at 405 nm. The decay spectra of these three samples are shown in Fig. 12. Multi-exponential decays are observed from the curvatures of the plots. These spectra are all well fitted by triple-exponential decay models, with χ^2 values close to 1 (Table 2). Their lifetimes and intensities are also listed in Table 2. The three lifetimes τ_1 , τ_2 and τ_3 of A8 are 0.934, 2.924 and 10.634 ns, respectively, and are longer than the corresponding lifetimes of g-C₃N₄ or Bi₂MoO₆, while maintaining similar lifetime intensities. These three lifetimes have intensities of ~24, ~47 and ~29%, respectively, of the total fluorescence intensity (Table 2). The prolonged lifetime originates from the formation

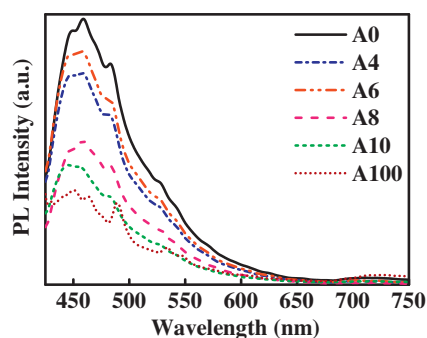


Fig. 11. PL spectra of g-C₃N₄ (A0), Bi₂MoO₆ (A100) and g-C₃N₄/Bi₂MoO₆ composites (A4–A10), recorded at an excitation wavelength of 405 nm.

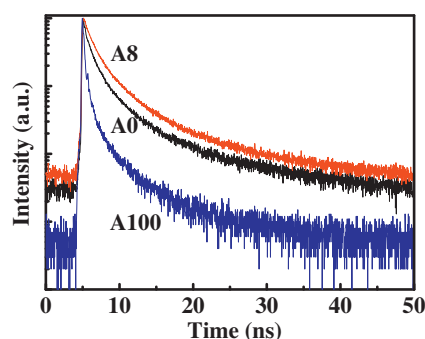


Fig. 12. Time-resolved fluorescence decay spectra of g-C₃N₄ (A0), Bi₂MoO₆ (A100) and g-C₃N₄/Bi₂MoO₆ composite A8 monitored at 460 nm by time-correlated single-photon counting, with an excitation wavelength of 405 nm.

of the g-C₃N₄/Bi₂MoO₆ heterojunctions, which effectively reduces the recombination of photogenerated electrons and holes.

The photoactivity enhancement of A8 is ascribed predominantly to the formation of the g-C₃N₄/Bi₂MoO₆ heterojunction. The specific surface area of A8 is more than twice that of g-C₃N₄ or Bi₂MoO₆, and this may be another factor for the photoactivity enhancement. The adsorbability of RhB or MB by the as-prepared photocatalysts is not a major factor, since the amounts of adsorbed dyes on these photocatalysts are comparable (Figs. S2 and S3a). h^+ , e^- , $\bullet O_2^-$ and $\bullet OH$ are all possible active species for the photodegradation of organic pollutants [47–49]. Photogenerated electrons from g-C₃N₄ and Bi₂MoO₆ could reduce surface chemisorbed O₂ to superoxide radicals ($\bullet O_2^-$) ($E(O_2/\bullet O_2^-) = -0.046$ eV vs. NHE) [50]. Hydroxyl radicals ($\bullet OH$) can be generated from $\bullet O_2^-$ [49]. To evaluate the role of these active species, individual scavengers were added to the photodegradation system. The scavengers used were tert-butyl alcohol (*t*-BuOH) for $\bullet OH$ [48], sodium oxalate for h^+ [47], K₂Cr₂O₇ for e^- [49] and benzoquinone (BQ) for $\bullet O_2^-$ [48]. Fig. 13 shows that the addition of *t*-BuOH or sodium oxalate causes a slight change in the photodegradation efficiency of A8. This indicates that $\bullet OH$ and holes are not significant active species in the

Table 2
Lifetimes (τ_1 , τ_2 and τ_3) and relative intensities (Int.) of g-C₃N₄ (A0), Bi₂MoO₆ (A100) and g-C₃N₄/Bi₂MoO₆ composite A8.

Samples	τ_1 (ns)/Int. (%)	τ_2 (ns)/Int. (%)	τ_3 (ns)/Int. (%)	χ^2
A0	0.707/24	2.468/47	10.166/29	1.230
A8	0.934/25	2.924/47	10.634/28	1.045
A100	0.125/22	0.775/48	4.976/30	1.791

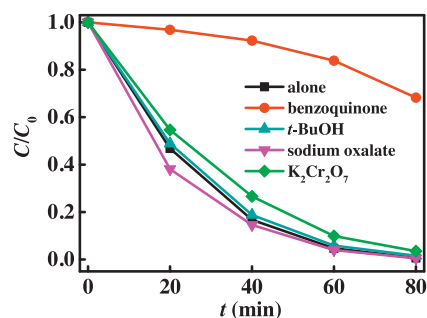
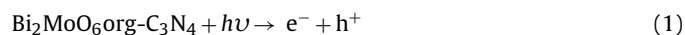


Fig. 13. Photocatalytic degradation of RhB over g-C₃N₄/Bi₂MoO₆ composite A8 with different scavengers: 20 mM t-BuOH, 0.2 mM sodium oxalate, 10 mM K₂Cr₂O₇ and 0.1 mM benzoquinone.

photocatalytic process. After K₂Cr₂O₇ is added, the photodegradation activity of A8 slightly declines, indicating that e[−] also plays a minor role. A significant suppression of photocatalytic performance is observed when BQ is added, confirming the important role of •O₂[−] in the photodegradation process. Thus, the photocatalytic process is mainly governed by •O₂[−], rather than by •OH, e[−] or h⁺, which is in agreement with the nature of the g-C₃N₄/Bi₂WO₆ composite [28].

According to the above discussion, the probable reactions occurring in the photodegradation of RhB are:



4. Conclusions

g-C₃N₄/Bi₂MoO₆ heterojunction photocatalysts were solvothermally prepared, and characterized by XRD, FT-IR, TG, XPS, TEM, HRTEM and SEM/EDS analyses. The heterostructure exhibited enhanced photodegradation efficiency for RhB and MB compared with g-C₃N₄ and Bi₂MoO₆. This resulted from a reduced photogenerated electron–hole recombination, caused by the transfer of holes from g-C₃N₄ to Bi₂MoO₆. The heterojunction composite with a Bi₂MoO₆ content of 16.1 wt.% exhibited the highest photocatalytic activity, and a less than 1% decline in activity was observed after six photocatalytic cycles. This heterostructure photocatalyst has potential in environmental remediation applications.

Acknowledgments

The present work is supported financially by the National Natural Science Foundation of China (no. 21173135) and the Specialized Research Fund for the Doctoral Program of Higher Education of China (no. 20110131130008).

Appendix A. Supplementary data

Supplementary data associated with this article can be found, in the online version, at <http://dx.doi.org/10.1016/j.apcatb.2014.05.019>.

References

- [1] A. Paracchino, V. Laporte, K. Sivula, M. Grätzel, E. Thimsen, *Nat. Mater.* 10 (2011) 456–461.
- [2] E.W. McFarland, H. Metiu, *Chem. Rev.* 113 (2013) 4391–4427.
- [3] L. Ye, L. Tian, T. Peng, L. Zan, *J. Mater. Chem.* 21 (2011) 12479–12484.
- [4] J. Tian, Y. Sang, G. Yu, H. Jiang, X. Mu, H. Liu, *Adv. Mater.* 25 (2013) 5075–5080.
- [5] D. Chen, M. Liu, Q. Chen, L. Ge, B. Fan, H. Wang, H. Lu, D. Yang, R. Zhang, Q. Yan, G. Shao, J. Sun, L. Gao, *Appl. Catal. B: Environ.* 144 (2014) 394–407.
- [6] L. Wei, Y. Chen, Y. Lin, H. Wu, R. Yuan, Z. Li, *Appl. Catal. B: Environ.* 144 (2014) 521–527.
- [7] W. Shi, J. Shi, S. Yu, P. Liu, *Appl. Catal. B: Environ.* 138–139 (2013) 184–190.
- [8] D. Wang, X. Chen, D.G. Evans, W. Yang, *Nanoscale* 5 (2013) 5312–5315.
- [9] J. Fu, B. Chang, Y. Tian, F. Xi, X. Dong, *J. Mater. Chem. A* 1 (2013) 3083–3090.
- [10] J. Xu, L. Zhang, R. Shi, Y. Zhu, *J. Mater. Chem. A* 1 (2013) 14766–14772.
- [11] Y. Hou, Z. Wen, S. Cui, X. Guo, J. Chen, *Adv. Mater.* 25 (2013) 6291–6297.
- [12] X. Wang, S. Blechert, M. Antonietti, *ACS Catal.* 2 (2012) 1596–1606.
- [13] Y. Wang, X. Wang, M. Antonietti, *Angew. Chem. Int. Ed.* 51 (2012) 68–89.
- [14] Y.-S. Jun, E.Z. Lee, X. Wang, W.H. Hong, G.D. Stucky, A. Thomas, *Adv. Funct. Mater.* 23 (2013) 3661–3667.
- [15] X. Wang, K. Maeda, A. Thomas, K. Takanabe, G. Xin, J.M. Carlsson, K. Domen, M. Antonietti, *Nat. Mater.* 8 (2009) 76–80.
- [16] Z. Hong, B. Shen, Y. Chen, B. Lin, B. Gao, *J. Mater. Chem. A* 1 (2013) 11754–11761.
- [17] S. Kumar, T. Surendar, A. Baruah, V. Shanker, *J. Mater. Chem. A* 1 (2013) 5333–5340.
- [18] M. Zhang, J. Xu, R. Zong, Y. Zhu, *Appl. Catal. B: Environ.* 147 (2014) 229–235.
- [19] N. Cheng, J. Tian, Q. Liu, C. Ge, A.H. Qusti, A.M. Asiri, A.O. Al-Youbi, X. Sun, *ACS Appl. Mater. Interfaces* 5 (2013) 6815–6819.
- [20] Y. Zhang, T. Mori, J. Ye, M. Antonietti, *J. Am. Chem. Soc.* 132 (2010) 6294–6295.
- [21] G. Liu, P. Niu, C. Sun, S.C. Smith, Z. Chen, G.Q. Lu, H.-M. Cheng, *J. Am. Chem. Soc.* 132 (2010) 11642–11648.
- [22] L. Sun, X. Zhao, C.-J. Jia, Y. Zhou, X. Cheng, P. Li, L. Liu, W. Fan, *J. Mater. Chem.* 22 (2012) 23428–23438.
- [23] S. Ye, L.-G. Qiu, Y.-P. Yuan, Y.-J. Zhu, J. Xia, J.-F. Zhu, *J. Mater. Chem. A* 1 (2013) 3008–3015.
- [24] C. Han, L. Ge, C. Chen, Y. Li, X. Xiao, Y. Zhang, L. Guo, *Appl. Catal. B: Environ.* 147 (2014) 546–553.
- [25] F. Yang, V. Kuznetsov, M. Lublow, C. Merschmann, A. Steigert, J. Klaer, A. Thomas, T. Schedel-Niedrig, *J. Mater. Chem. A* 1 (2013) 6407–6415.
- [26] S. Wang, D. Li, C. Sun, S. Yang, Y. Guan, H. He, *Appl. Catal. B: Environ.* 144 (2014) 885–892.
- [27] J. Fu, Y. Tian, B. Chang, F. Xi, X. Dong, *J. Mater. Chem.* 22 (2012) 21159–21166.
- [28] Y. Tian, B. Chang, J. Lu, J. Fu, F. Xi, X. Dong, *ACS Appl. Mater. Interfaces* 5 (2013) 7079–7085.
- [29] M. Shang, W. Wang, J. Ren, S. Sun, L. Zhang, *Nanoscale* 3 (2011) 1474–1476.
- [30] G. Tian, Y. Chen, W. Zhou, K. Pan, Y. Dong, C. Tian, H. Fu, *J. Mater. Chem.* 21 (2011) 887–892.
- [31] J.-P. Zou, S.-L. Luo, L.-Z. Zhang, J. Ma, S.-L. Lei, L.-S. Zhang, X.-B. Luo, Y. Luo, G.-S. Zeng, C.-T. Au, *Appl. Catal. B: Environ.* 140–141 (2013) 608–618.
- [32] Y.-S. Xu, W.-D. Zhang, *Appl. Catal. B: Environ.* 140–141 (2013) 306–316.
- [33] M. Zhang, C. Shao, J. Mu, X. Huang, Z. Zhang, Z. Guo, P. Zhang, Y. Liu, *J. Mater. Chem.* 22 (2012) 577–584.
- [34] S.C. Yan, Z.S. Li, Z.G. Zou, *Langmuir* 26 (2010) 3894–3901.
- [35] S. Martha, A. Nashim, K.M. Parida, *J. Mater. Chem. A* 1 (2013) 7816–7824.
- [36] J.M. Fernández, C. Barriga, M.A. Ulibarri, F.M. Labajos, V. Rives, *Chem. Mater.* 9 (1997) 312–318.
- [37] F. Trifiro, H. Hoser, R.D. Scarle, *J. Catal.* 25 (1972) 12–24.
- [38] Y. Cui, J. Zhang, G. Zhang, J. Huang, P. Liu, M. Antonietti, X. Wang, *J. Mater. Chem.* 21 (2011) 13032–13039.
- [39] Y.S. Xu, W.D. Zhang, *Dalton Trans.* 42 (2013) 1094–1101.
- [40] T. Li, L. Zhao, Y. He, J. Cai, M. Luo, J. Lin, *Appl. Catal. B: Environ.* 129 (2013) 255–263.
- [41] S. Cho, J.-W. Jang, K.-j. Kong, E.S. Kim, K.-H. Lee, J.S. Lee, *Adv. Funct. Mater.* 23 (2013) 2348–2356.
- [42] J.L. Gunjakar, I.Y. Kim, J.M. Lee, N.S. Lee, S.J. Hwang, *Energy Environ. Sci.* 6 (2013) 1008–1017.
- [43] Y. Chen, R. Huang, D. Chen, Y. Wang, W. Liu, X. Li, Z. Li, *ACS Appl. Mater. Interfaces* 4 (2012) 2273–2279.
- [44] M.R. Hoffmann, S.T. Martin, W. Choi, D.W. Bahnemann, *Chem. Rev.* 95 (1995) 69–96.
- [45] H. Li, Q. Deng, J. Liu, W. Hou, N. Du, R. Zhang, X. Tao, *Catal. Sci. Technol.* 4 (2014) 1028–1037.
- [46] D. Jiang, L. Chen, J. Zhu, M. Chen, W. Shi, J. Xie, *Dalton Trans.* 42 (2013) 15726–15734.
- [47] X. Xiao, R. Hu, C. Liu, C. Xing, C. Qian, X. Zuo, J. Nan, L. Wang, *Appl. Catal. B: Environ.* 140–141 (2013) 433–443.
- [48] L. Mohapatra, K. Parida, M. Satpathy, *J. Phys. Chem. C* 116 (2012) 13063–13070.
- [49] S. Ge, L. Zhang, *Environ. Sci. Technol.* 45 (2011) 3027–3033.
- [50] D. Zhang, J. Li, Q. Wang, Q. Wu, *J. Mater. Chem. A* 1 (2013) 8622–8629.